LCF behaviour and a comprehensive life prediction model for AlSi10Mg obtained by SLM

S. Romano, L. Patriarca, S. Foletti, S. Beretta*

Politecnico di Milano, Department of Mechanical Engineering, Via La Masa 1, I-20156 Milan, Italy

The full potential of additive manufacturing (AM) components is today yet to be reached. Space and aerospace industries are still conservative in the use of AM parts for safety–critical applications, mostly because of the uncertainties and low reproducibility that are often associated with the process. One of the most challenging issues is the fatigue resistance. The rough surface condition and the presence of manufacturing defects can cause significant scatter, leading to the adoption of large conservative safety factors. To robustly model the fatigue resistance of defected AM materials, there is a need to implement defect-tolerant designs and deal with these uncertainties. The present research activity aims at developing a model for fatigue life estimation in a large range of loading conditions, from high cycle fatigue to low cycle fatigue. This is achieved by adopting a fracture mechanics approach, through elastic–plastic fatigue crack growth calculations based on the known defect population inside the material. The model has been applied to AlSi10Mg produced by three slightly different selective laser melting processes, showing a robust estimation of fatigue life and scatter with limited experi-mental effort. The life predictions performed are then summarised in design maps where the allowable stress (or strain) depends on the defect size and on the HCF/LCF design upon the number of cycles selected.

Keywords:
AlSi10Mg
Additive manufacturing
Low cycle fatigue
Elastic–plastic driving force
Defects

1. Introduction

In the recent years, additive manufacturing (AM) has introduced outstanding opportunities for various applications. The fundamentals and working principles of AM offer several advantages, including significant material and mass saving, near-net-shape capabilities, superior design, geometrical flexibility and significant reduction of concept-to-validation time [1]. These advantages have raised the interest of space and aerospace companies, as well as automotive, medical, and energy industries. The possibility to significantly reduce fuel consumption and emissions, the increased payload allowed by important weight saving and the massive reduction of the fly-to-buy ratio [2] have caused space and aerospace industries to take the lead in the design and verification of these parts.

The long-term goal is to directly qualify the process and materials and to obtain a fast and robust process flow from concept to part verification. At the moment, this is still not yet fully achieved, and the verification of structural parts is performed on the particular case-study, which usually implies large time and costs. However, the development of holistic process flows has demonstrated the capability to reduce the time from concept to verification for flight to almost eight weeks, with aggressive testing campaign to guarantee the project spe-cifications are met [3].

Despite the many advantages of AM and the rapid, continuous improvements in the process, the high stakes involved creates apprehension and conservatism among many industry leaders regarding the readiness of the technology for structural flight parts. One of the main limiting drawbacks is the difficulty to achieve good and stable material quality. This mainly refers to the poor surface roughness and compliance to strict tolerances and to the ineluctable presence of manufacturing defects.

The problem of obtaining a good surface finishing without resorting to standard manufacturing is currently being investigated by many research groups in academia and industries. Among the several possibilities, there are chemical or electrochemical etching [4], sand blasting, micro shot-peening, and vibratory polishing [5], or laser ablation during the process [6]. At the same time, the producers of AM machines are constantly improving the final quality that can be obtained from the process [7,8].

Considering manufacturing defects, the size of these flaws has considerably decreased in recent years [9], and further improvements may still be possible through adequate process control. At the same time, the main concern for industries is more to speed up the process than to completely eliminate defects. Hot isostatic pressing (HIP) guarantees almost complete elimination of the voids, but the use of this

* Corresponding author.
E-mail address: stefano.beretta@polimi.it (S. Beretta).

Published Journal Article available at: https://doi.org/10.1016/j.ijfatigue.2018.07.030

Nomenclature

a	crack depth
c	surface crack length
da/dN	crack propagation rate
d_g	sample gauge diameter
l_g	sample gauge length
C, n, p	NASGRO equation parameters
E	Young's modulus
E'	Young's modulus for plane strain condition
K', n'	Ramberg–Osgood parameters
N_f	number of cycles to failure
$N_{k,\sigma}$	knee-point of the Wöhler curve
P_J	crack length independent damage parameter
R	stress ratio
R_ϵ	strain ratio
R_m	tensile strength
$R_{p,0.2}$	0.2% proof strength
$R^c_{p,0.2}$	stabilised cyclic yield strength
Y	boundary correction factor for SIF calculation
α	constraint factor
ϵ	strain level
ν	Poisson's ratio
σ	stress level
σ_0	flow stress
σ_{cl}	closing strain level
$\sigma_{\max}$	maximum applied stress
σ_{op}	opening stress level
σ'_f, ϵ'_f, b, c	Coffin-Manson parameters
ΔJ	cyclic J-integral range
ΔK	SIF range
$\Delta\epsilon$	strain range
$\Delta\sigma$	stress range
$\Delta\sigma_{w0}$	fatigue limit in absence of defects

Acronyms

AM	additive manufacturing
COD	crack opening displacement
CT	computed tomography
DIC	digital image correlation
EPFM	elastic–plastic fracture mechanics
FCG	fatigue crack growth
HCF	high cycle fatigue
LCF	low cycle fatigue
LEFM	linear-elastic fracture mechanics
RO	run-out
SEM	scanning electron microscope
SIF	stress intensity factor
SLM	selective laser melting
VA	variable amplitude

Indices

0	initial value
a	amplitude
cl	closure
eff	effective
el	elastic
f	final value
lc	long crack
max	maximum
op	opening
pl	plastic
th	threshold

technique is limited due to the high cost and complexity. Depending on the material, the presence of defects could significantly decrease the fatigue properties, even for small dimensions (e.g., of the order of 100 μm in terms of diameter). Despite this reduction in fatigue resistance not being a limiting factor in many applications, the designer still has to deal with defect-tolerant concepts and assessments.

Further issues related to AM are the large scatter often associated with experimental fatigue data and the poor repeatability. This generally involves the need for extensive fatigue testing campaigns to robustly assess the resistance of every build of material, as well as the adoption of excessive safety factors to cover the risk of *unknown unknowns* [10]. In order to solve these issues, a thorough understanding of the material behaviour under fatigue loading, together with probabilistic approaches to deal with uncertainties, are needed [11–13].

A literature review of two of the most used lightweight alloys in the space and aerospace sectors (AlSi10Mg and Ti-6Al-4V) [14] showed the applicability of the Kitagawa diagram [15] for assessing the fatigue limit of parts containing manufacturing defects. The defects can indeed be treated as short cracks at stress levels close to the fatigue limit. The scatter is a combination of the inherent variability and dependence on the defect size, which can be simply described by the Murakami's $\sqrt{\mathrm{area}}$ parameter [16]. The application of these concepts [9] has shown that fatigue resistance and experimental scatter are mainly controlled by the most detrimental defect present in the material. The most important variables to assess the critical defect size are the applied stress, the defect $\sqrt{\mathrm{area}}$ and the distance from the surface. More complex models including the effect of defect shape, proximity of other defects and plastic-strain concentration have also been adopted with limited improvements [17]. The determination of the critical defect size for a given volume of material can be obtained through statistical investigations of X-ray computed tomography (CT) measurements [18].

Finally, it has been shown that finite life in the elastic field can be predicted by fatigue crack growth (FCG) simulations based on linear-elastic fracture mechanics (LEFM), while plasticity plays an important role at higher stresses and elastic–plastic fracture mechanics (EPFM) shall be used.

Therefore, the present work aims at extending the approach developed in [9] for HCF of AlSi10Mg, obtained by AM, to the low cycle fatigue (LCF) regime through an elastic–plastic definition of the driving force ahead of the manufacturing defects. The goal is to develop a single model able to describe the fatigue resistance of an AM material from the HCF threshold condition to LCF.

1.1. Elastic–plastic fracture mechanics

Although most proof test analyses reported in the open literature successfully employed LEFM, it is now recognised that a proof test analysis should be based on EPFM [19]. Conventional fatigue crack propagation approaches rely on the relationship between the stress intensity factor range and crack growth rate, whose application is limited by small-scale yielding conditions. Outside the small-scale yielding limits, the applicability of a parameter derived from a linear theory decays, and the stress intensity factor range shall be substituted by a crack driving force parameter of elastic–plastic fracture mechanics [20]. This becomes very important when assessing components, most of which are subjected to a large range of stress and strain cycles.

Considering space parts, for example, there are multiple load cases to be considered for the fatigue assessment (e.g., transportation, launch, on-orbit unloading, normal operation, thermal cycles, etc.). Similar considerations can be done for aerospace applications, as well as for automotive, energy, medical, etc. If most of these loading cycles can be irrelevant for fatigue damage, some loads can make fatigue cracks

nucleate and propagate. The ability to predict the structural damage during the life cycle of the part is then a very important asset, especially considering various loading conditions and variable amplitude (VA) loading. The standard assessment for VA loading is based on cumulative damage models (e.g., Miner rule [21]), which are simple but sometimes not very accurate [22]. Improved prediction accuracy has been achieved for cases where the effects of the load history are incorporated into the analysis: the models based on the transient elasto-plastic fa-tigue damage offer higher precision [23–26].

Dealing with LCF resistance may also be necessary in the assessment of structures where stress raisers (e.g., sharp corners or notches) can cause local plasticity [27]. A limited amount of research focusing on the LCF resistance of AM material is available in the literature. Among the materials investigated, there are Ti alloys (Ti-6Al-4V [28–30] and TC18 [31]), AISI 316L [32] and Inconel 718 [33,34]. However, to the authors knowledge, no research has been conducted on AlSi10Mg except a preliminary investigation by the authors [35]. Some of the important results of these activities are recurrent short LCF lives compared to wrought material due to lower ductility [30,36], negligible crack nucleation time [37,38], numerous crack initiation sites and possible defect clustering effects [9,31,32,36] and significant influence of residual stresses [28] and anisotropy [34] on the cyclic behaviour. Aydinöz et al. [33] experienced strong asymmetrical behaviour in Inconel 718 after solution annealing and ageing treatments, which may fully or partially decrease with continued cyclic loading.

For the reasons discussed, this paper investigates the LCF resistance of AlSi10Mg specimens produced by selective laser melting (SLM). To broaden and validate the model, the material tested was manufactured by three different processes. The research is constructed on the top of two pillars: (i) the fatigue properties of AM materials appear to be controlled by the manufacturing defects close to the surface [30,32,36,39] and the fracture mechanics tools already available can be used for defect tolerant design [9,14,18]; (ii) modelling the fatigue life through the elasto-plastic crack driving force incorporating crack closure concepts leads to satisfactory prediction accuracies both in the LCF and HCF regimes [20,23]. This approach enabled the generalisation of the classical Kitagawa diagram for HCF design into defect-tolerant maps which, provided the number of cycles ranging between the HCF and the LCF regimes, report the allowable stress (or strain) as a function of the defect size.

The paper is organized as follows. Firstly, the experimental details of the research are reported in Section 2. The LCF results are then presented in Section 3, highlighting the evidence that manufacturing defects control the fatigue behaviour when a proper surface finish is ensured. The analysis of LCF through the adoption of ΔJ_{eff} model is the objective of Section 4, with a detailed discussion of the effect of defects on fatigue properties in Section 5.

2. Experimental details

2.1. Material

The experimental activity was based on samples fabricated by SLM using the aluminium alloy AlSi10Mg. Five series of cylinders were produced on an EOS M400 powder-bed machine between 2015 and 2017. An inner hatch filling strategy was adopted for all the samples. The contouring on the surface was not necessary, as the diameter of the cylinders was halved by machining to reach the final gauge diameter. The samples were produced by three processes, referred to as process 1 to process 3 (P1-P3). The same SLM machine, powder, and manufacturing parameters were adopted for P1 and P2. Therefore, no remarkable differences are expected between these processes. However, owing to the rapid development of SLM technology, the recirculating inert gas system required to remove released gas and particles was improved in the meantime. P3 was optimized with the aim of im-proving the fatigue resistance. The two parameters modified with respect to the previous processes were the layer thickness (reduced from 60 μm to 30 μm) and the platform pre-heating temperature (re-duced from 200 °C to 165 °C) [5]. The porosity values calculated by CT scan resulted 0.12% to 0.28% for P1, 0.15% to 0.38% for P2, and 0.02%to 0.04% for P3. The details of the manufacturing parameters adopted are reported in Table 1.

Table 1
AM processing parameters adopted for the three processes (∗ data not disclosed due to confidentiality agreement with the manufacturer).

SLM process parameter	P1	P2	P3
Laser beam power (W)	1000	1000	∗
Energy input (J mm^{-3})	∗	∗	50
Laser beam focus diameter (μm)	90	90	90
Layer thickness (μm)	60	60	30
Pre-heating temperature of the platform (°C)	200	200	165

Two different orientations have been investigated, placing the specimen's axis parallel or perpendicular to the building direction. These will be referred to as vertical (V) and horizontal (H), respectively. None of the parts received any final heat treatment; however, significant residual stresses were not expected owing to the platform pre-heating.

The microstructure was analysed by observing polished cross-sections with optical microscopy, considering all the processes and orientations investigated. Chemical etching was performed applying Keller's reagent (95 mL water, 2.5 mL HNO_3, 1.5 mL HCl, 1.0 mL HF) for 10 s, the results are depicted in Fig. 1. The micrographs indicate the typical half-cylindrical shape of the melt pools, as well as the presence of some voids. More details about the microstructure of AlSi10Mg alloy are reported in [40,41], which show a microstructure very similar to the one investigated, constituted by fine *nanocells*. Based on these analyses, it was determined that a short crack regime can be adopted when the size of the detrimental defects is large enough with respect to the microstructural features (i.e., approximately larger than 100 μm). Therefore, a fracture mechanics assessment of these defects can be adopted [9].

2.2. Static properties

The static tests performed on the three processes investigated have been described in [9], and the results are summarised in Table 2. The data show an increase in both the yield stress $R_{p,0.2}$ and ultimate tensile stress R_m between P1 and the other two processes. At the same time, the variability between the different samples decreased, confirming the process improvement. In all cases, these static properties outperform those obtainable by casting. Even the maximum strain at failure is reasonably high, as it reaches 6.4–7.2% for the horizontal samples and slightly lower values for the vertical orientation. As the elongation to failure was repeatable, the possible reasons for the differences in strength between P1 and P2 is most likely caused by a different thermal history. In fact, it is known that the gas shielding has the double effect of reducing the spattering phenomena as well as influencing the cooling rate of the melt pool [42]. As for the defects, their influence with respect to static resistance is expected to be small.

2.3. Residual stress measurements

The presence of residual stresses due to the manufacturing process was investigated by X-ray diffraction. The measurements were performed on one vertical sample from P2 along a path perpendicular to the building direction.

Electro-polishing technique was adopted to achieve a 400 μm material removal with a step-by-step procedure. Two diametrically opposed points on the gauge volume were investigated. Electro-polishing was performed on a circular area with a diameter of 5 mm by using an

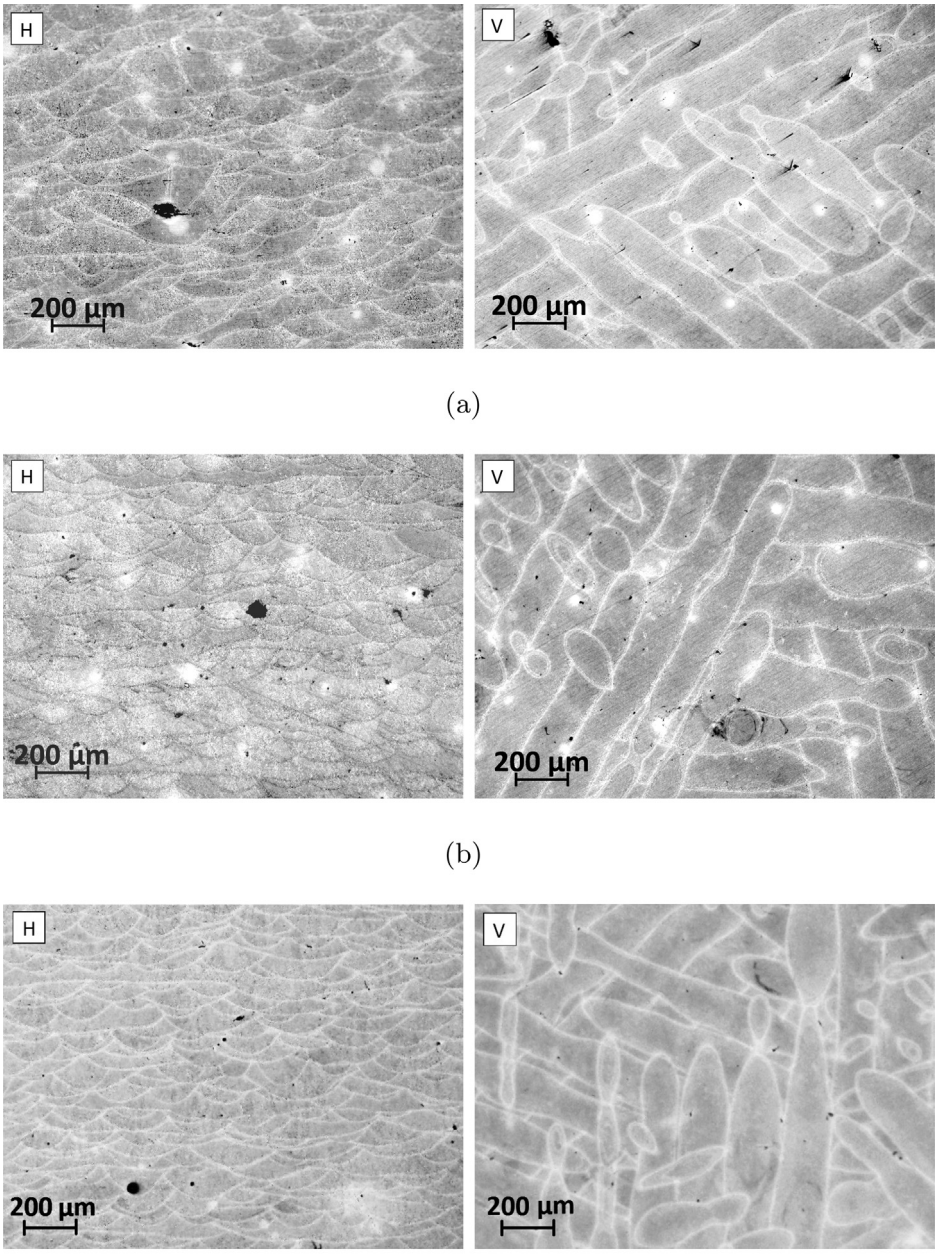

Fig. 1. Optical micrography after chemical etching for H and V material orientations (from [9]): (a) P1; (b) P2; (c) P3.

Table 2
Summary of the AlSi10Mg tensile properties [9].

Process	Orientation		E (GPa)	$R_{p,0.2}$ (MPa)	R_m (MPa)	A% (%)
P1	Horizontal	Average	73.3	224.9	365.3	6.8
		std. dev.	0.4	4.8	4.9	0.4
	Vertical	average	72.6	236.3	406.4	5.3
		std. dev.	0.2	16.7	5.0	0.4
P2	Horizontal	Average	74.6	304.5	441.5	6.7
		std. dev.	0.1	0.7	0.7	0.1
P3	Horizontal	Average	70.2	291.0	443.7	6.6
		std. dev.	1.8	3.8	3.2	0.4
	Vertical	average	72.8	253.7	440.2	3.0
		std. dev.	2.3	2.3	4.9	0.2

electrolytic solution of 94% CH_3COOH, 6% $HClO_4$ at a voltage of 35 V. A precision Mitutoyo micrometer (IDCH0530/05060) was used to in-sure that a 100 µm material removal was reached at each step.

The X-ray diffractometer adopted was a portable AST X-Stress 3000, CrK-α radiation, $\sin^2(\psi)$ method. The diffraction angle considered was 139°, with 30 s exposure time and 3 tilts in the range $-45°$ to 45° along three rotations of 0° (specimen axis direction), 45° and 90° (radial direction).

The results obtained are depicted in Fig. 2. The low precision and resolution of the measurements does not allow for robust quantification of the stresses. However, the trend shows a repeatable compressive residual stress close to the surface, which then quickly increases to zero or slightly positive values. These results are consistent with the ones reported by Bagherifard et al. [43] for the same alloy in the as-built condition, except for the compressive stress found on the surface, which was not detected in that case. The reason for this is likely to be the

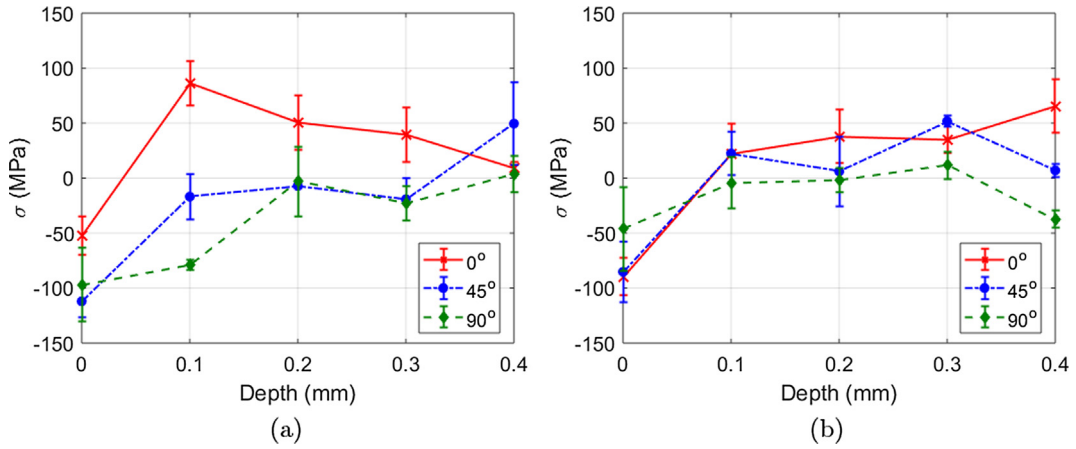

Fig. 2. Distribution of residual stresses on P2: (a) point 1; (b) point 2.

effect of turning, which can introduce some small compressive stress in the first layers of machined samples. The measurements confirm an almost complete removal of residual stresses achieved by platform preheating. Note that the axial results for the horizontal orientation are described by the 90° direction and show a quick stabilisation to zero stresses.

2.4. Fatigue tests

The LCF response of AlSi10Mg obtained by selective laser melting was investigated by performing axial strain-controlled tests on an MTS 810 servohydraulic machine, with a frequency of 0.5 Hz. A strain ratio $R_\epsilon = -1$ was applied, and the strain was measured using a clip-on gauge extensometer with 10 mm gauge length. All fatigue samples were designed according to ASTM E606 standard [44]. The relevant dimensions of the cylindrical specimens are: gauge length $l_g = 16$ mm, diameter $d_g = 6$ mm and gauge volume $V_g = 452$ mm^3. The majority of the strain-controlled tests were carried out on samples from P1 and P2. Few specimens of P3 were investigated, as this material showed a cyclic response very similar to the one of P2. The S-N curves of the three batches were investigated by a series of axial force-controlled tests, which were reported and analysed in [9]. The results obtained in fully elastic loading conditions have been considered in the following to obtain a complete description of the $\epsilon-N_f$ curves. A comprehensive overview of the tests performed is reported in Table 3.

As the aim of this study is the assessment of AM parts in relation to the presence of manufacturing defects, all the specimens have been machined to avoid the detrimental effect of the surface roughness. The final surface roughness was measured with a profilometer, yielding $R_a = 0.33$ μm and $R_z = 2.99$ μm.

2.4.1. Tests with artificial defects

A common observation in literature is that the fatigue failure of machined AM samples is usually caused by surface or subsurface voids [18,45–47]. To define a safe reference fatigue life curve, artificial micro-notches were introduced in the center of the gauge volume of some samples. The experimental investigations have shown similar fatigue results for defects having similar area, but different shapes [16]. Applying the concepts described in [18], the area of the artificial defects was determined as a safe percentile (i.e., 97.5%) of the maximum defect distribution in the surface gauge volume. The dimensions of the artificial defects obtained are summarized in Table 4, and the geometries are depicted in Fig. 3. The micronotches in P1 were introduced by milling, whereas femtosecond laser was adopted as described in [48] for P2 and P3 due to the small dimensions required.

2.5. Fatigue crack growth properties

The FCG properties of the material have been reported in [9]. The first set of tests performed investigated FCG in the absence of crack closure. The tests were carried out on Compact tension (C(T)) specimens from P2 at a stress ratio $R = 0.7$, considering the most detrimental crack propagation direction (i.e., crack parallel to the manufacturing layer). The $da/dN-\Delta K_{\text{eff}}$ curve obtained is the input for the life predictions based on ΔJ_{eff} concepts, which are discussed in Section 4.

Cyclic resistance-curve tests on single edge notched tensile specimens were also carried out on the P2 process in order to precisely measure the crack propagation threshold at $R = -1$. The crack propagation threshold resulted to be $\Delta K_{th,lc}$ 3.2–3.6 MPa m . For all the details of the resistance-curve assessment, see [49,50].

2.6. Measurements of crack development and growth under LCF

Digital Image Correlation (DIC) has been used to evaluate the development of local plastic deformation in the material under LCF conditions. A first set of two experiments was performed measuring the local strain fields on a flattened fatigue specimen from P1 along the horizontal and vertical orientations. The aim of these tests was to verify the amount of local plastic deformation around the manufacturing defects and quantify the effective crack incubation time. These experiments aimed to provide a better understanding of crack nucleation and propagation in LCF regime. An applied strain amplitude $\epsilon_a = 0.38\%$ was selected for the tests to guarantee a good balance between the amount of plastic deformation and the fatigue life of the sample.

A second set of LCF experiments was performed on flattened specimens from P2 with artificial defects. The aim of these tests was to evaluate the displacement field around a propagating crack during the LCF cycles in order to measure crack opening and closure levels during propagation. Three strain amplitudes were selected: $\epsilon_a = 0.26\%$, which determines a dominant elastic material behaviour, $\epsilon_a = 0.3\%$ and $\epsilon_a = 0.38\%$, which promote large plasticity. The results of these experiments aim to validate the crack closure model adopted in the present life prediction model and are described in Section 3.4.

The specimens were machined according to the cylindrical geometry described in Section 2.4. The central part of the specimens was

Table 3
Summary of the fatigue tests performed on the present AlSi10Mg alloy.

Process	Strain-controlled	Load-controlled
P1	22	18
P2	36	45
P3	7	42

Table 4
Summary of artificial defects dimensions in terms of $\sqrt{area}$.

Process	Average $\sqrt{area}$	Std. deviation
P1	374	55
P2	290	57
P3	150	15

successively machined in order to obtain two parallel surfaces required for the DIC measurements. The flattened surface was initially polished via emery paper up to a grit size of P1600. The speckle pattern was introduced by airbrushing a black paint using an Iwata airbrush with a nozzle diameter of 0.18 mm. The images were captured by a 2 megapixel Allied vision Manta G201B digital camera and a set of lens produced by Optem which yielded a final adjustable magnification from 10× to 65×. The magnification adopted in the measurements was set to 0.9 μm/px. The combination between the quality of the speckle pattern and the lens magnification yielded the adoption of a subset size of approx. 70 μm. These DIC settings allowed for locating the local strain variations induced by the manufacturing defects for the LCF nucleation tests, which are characterized by a size of the order of 50–250 μm in terms of $\sqrt{area}$. It is important to remark that the image acquisition strategy changes according the type of test. In this case, the goal was to locate the most detrimental manufacturing defect in the LCF nucleation test. This was achieved considering an area of 3.73 mm × 5 mm for the DIC measurements, which represents the observable region in the extensometer gauge space. The magnification was set to obtain a target resolution of 0.9 μm/px, which guarantees sufficient spatial resolution to capture the strain localization arising from the manufacturing defects. At this magnification, the region of interest (ROI) is 1.5 mm × 1.14 mm; multiple images were then required to cover the target area. A set of 21 images was initially captured to define the reference images for the correlation before specimen deformation. Successively, the tests were interrupted at zero strain in the upward branch of the hysteresis cycle in order to capture the deformed images. The pictures were then correlated and stitched together to obtain the strain maps at specific test interruptions, which were used as damage maps indicating the development of cracks in the material. Additional correlations were also implemented by continuum real-time acquisition of a specific specimens areas. In these cases, the microscope was positioned at specific specimen locations (for example, the micro-notch area in the LCF propagation tests) and a video was captured for the entire hysteresis cycle. A Labview program was used to acquire and synchronize the load cell and the extensometer signals with the images extracted from the video. The correlations were then performed using the image at the minimum load as reference. The strain maps obtained from these measurements were then used to (i) study and compare the local strains arising from the manufacturing defects in the LCF nucleation tests for the horizontal and vertical orientations; (ii) detect the crack tip position in the LCF propagation tests and then measure the crack propagation rate. An example of vertical (axial) strain maps used to locate the crack tip position is shown in Fig. 4a. The propagation

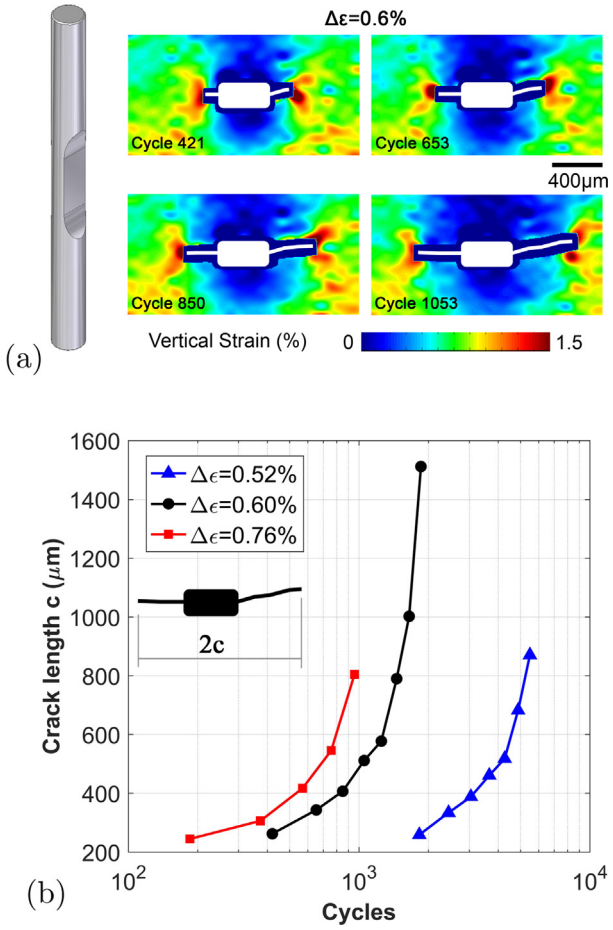

Fig. 4. DIC investigation on a micro-notched P2 specimen tested at $\Delta\epsilon = 0.6\%$: (a) sketch of the specimen geometry and sequence of DIC maps of axial strain ϵ_y in proximity of the micro-notch; (b) measured crack advancements for the tests conducted at $\Delta\epsilon = 0.52\%$, $\Delta\epsilon = 0.6\%$ and $\Delta\epsilon = 0.76\%$.

curves (Fig. 4b) were then used to calculate the crack growth rates.

In addition to these tests, the crack growth rates at $R = -1$ for both P1 and P2 have been evaluated measuring the surface crack length increment by means of replica technique and optical microscopy. These results were necessary to verify the ability of the model to estimate the crack growth rates at $R_\epsilon = -1$ in presence of plasticity based on the effective elastic FCG data, which is the topic of Section 4.2.

3. Low Cycle Fatigue properties

3.1. Cyclic response

The cyclic behaviour of the present AlSi10Mg alloy shows an initial

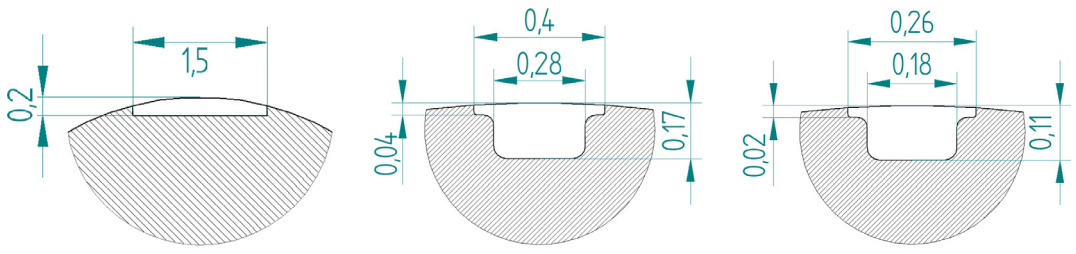

Fig. 3. Drawings of the artificial defects introduced in the samples: (a) P1; (b) P2; (c) P3.

softening and a fast stabilisation of the peak and valley stress in the first 2–3% of fatigue cycles. This behaviour was observed for all the specimens and processes. Considering different material orientations, slightly negative mean stress was observed in most vertical specimens, whereas this was not evident for the horizontal orientation. This is a common behaviour in all of the processes (see Fig. 5a–c), but the scatter in the cyclic properties is too small and the number of tests performed isn't large enough to statistically ensure the presence of a significant trend. Therefore, all the specimens belonging to the same process have been investigated together. Similar asymmetric response has been re-ported by Agius et al. [28] considering Ti-6Al-4V produced by SLM, mostly for the H orientation. This can probably be attributed to slight residual stresses and anisotropy due to the manufacturing process, which can influence the material ductility and introduce scatter in the cyclic yield strength [28,34], as clearly depicted in Fig. 9.

The stabilised hysteresis loops have been collected and a Ramberg–Osgood [51] equation has been fitted to this data, as shown in Fig. 5d. The average cyclic yield strength, $R^c_{p,0.2}$, and the Ramberg–Osgood coefficients fitted on the various material and orientations investigated are summarised in Table 5. It can be noted that the scatter between the points belonging to the same process results relatively small. The cyclic yield strength $R^c_{p,0.2}$ increases significantly from P1 to P2, while no visible differences are detected between P2 and P3 up to the maximum strain range investigated $\Delta\epsilon_{app} = 1\%$.

3.2. Fatigue life

The results of the strain-controlled fatigue tests performed are depicted in Fig. 6a, which shows that P1 has the lowest fatigue resistance, while P3 has the best properties. Process P2, instead, is characterised by an intermediate resistance and the largest variability. These results are in accordance with those obtained by Romano et al. [9] investigating the HCF resistance. The main reason behind the different resistance in HCF has been attributed to the defect size, which was seen to decrease from P1 to P3. In fact, normalising the applied stress while accounting for the killer defect size made possible to eliminate the scatter between the fatigue resistance of the three processes.

The killer defect size has a strong influence even in LCF. In fact, a shorter life is usually associated with a larger defect at the fracture origin in case of LCF tests for the same strain amplitude and batch. Note that in the presence of plastic deformation a different cyclic response at the same strain amplitude has been observed for different processes. As a consequence, a comparison between the different processes can be performed considering the different cyclic behaviour.

With the aim of obtaining a comprehensive relationship to describe the fatigue resistance in the whole range of applicable strains, the strain applied to the HCF samples tested in the fully-elastic regime has been calculated, and these data have been combined with the LCF results. Finally, a Coffin-Manson relationship (Eq. (1)) [52,53] has been fitted to the data related to natural defects (see Fig. 6b), and the four parameters resulting from the fit (σ'_f b, ϵ'_f and c) for the three processes are summarised in Table 6.

$$\epsilon_a = \epsilon_{a,el} + \epsilon_{a,pl} = \frac{\sigma'_f}{E}(2N_f)^b + \epsilon'_f\ (2N_f)^c \tag{1}$$

In Section 3.1, it has been pointed out that the stabilised cyclic response of a batch of material has limited variability. This observation allows to describe all the specimens belonging to the same process with a unique Ramberg–Osgood equation with negligible error. Moreover, as the peak stress stabilisation takes place in a few cycles at the beginning of the strain-controlled tests, the cyclic response of the material can be simply modelled considering only the stabilised cyclic curve, i.e., neglecting the initial softening. This engineering assumption allows the use of the RO relationship to calculate the strain amplitude to be applied to cause the same fatigue damage that a given applied stress amplitude would cause. In this way, the force-controlled test results can

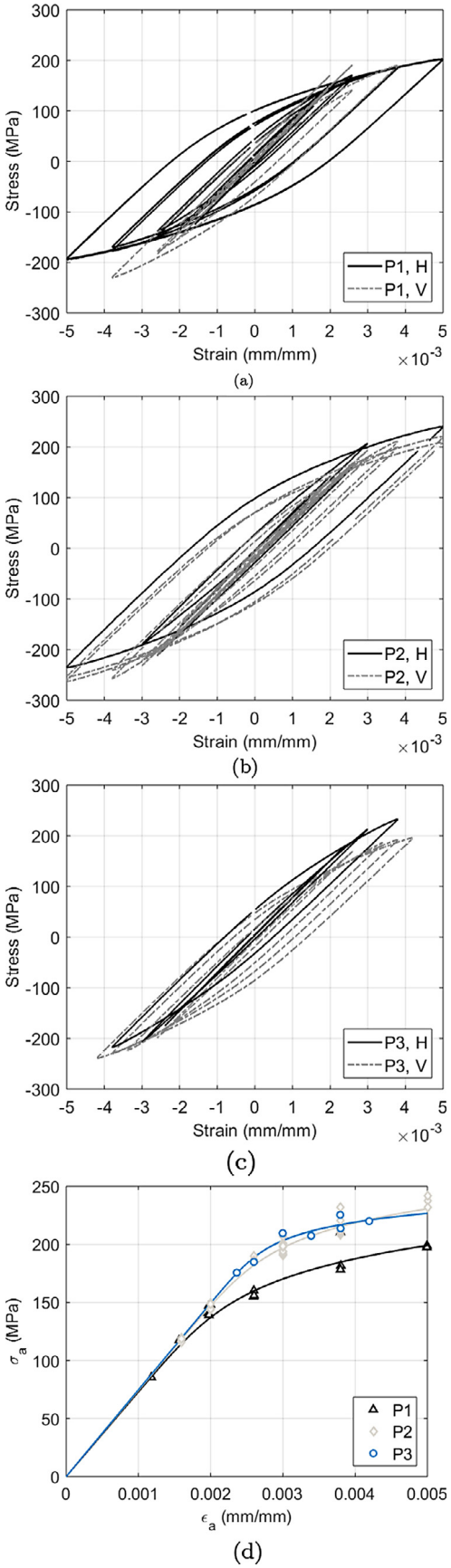

Fig. 5. Cyclic response of the material: stabilised hysteresis loops for H and V orientation for (a) P1; (b) P2; (c) P3. (d) Stabilised cyclic response comparison and Ramberg–Osgood fit for the three processes.

Table 5
Summary of the Ramberg–Osgood coefficients fitted on the experimental stabilised cyclic curves and their 90% confidence (confidence band for P3 not significant because calculated on a few data).

Process	E (GPa)	$R^c_{p0.2}$ (MPa)	K' (MPa)	n'
P1	73.0	195.7	434 (363–518)	0.128 (0.105 0.157)
P2	74.1	231.8	410 (347–484)	0.092 (0.069 0.114)
P3	74.7	226.9	321 (∗)	0.056 (∗)

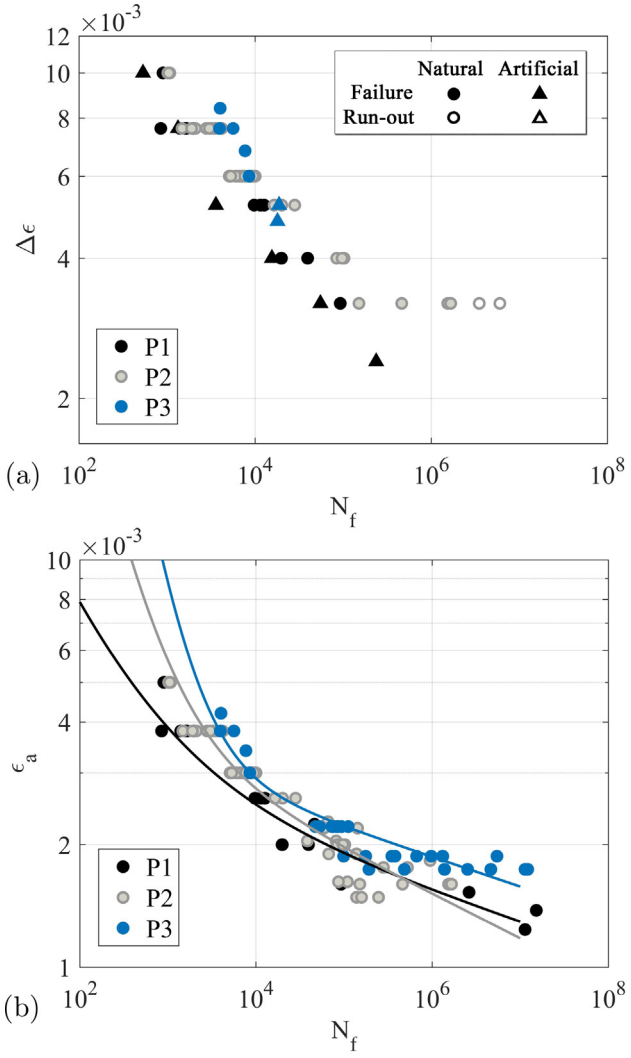

Fig. 6. Fatigue test results: (a) ϵ-N strain-controlled tests; (b) Coffin-Manson data fit.

Table 6
Summary of the Coffin-Manson coefficients fitted on the experimental data.

Process	σ'_f	b	ϵ'_f	c
P1	327.5	−0.074	0.097	−0.564
P2	552.0	−0.110	5.534	−1.017
P3	401.8	−0.073	101.7	−1.287

be plotted in terms of applied strains together with the LCF results.

The experimental observation that fatigue failures originated from surface or sub-surface defects in HCF is confirmed even in presence of large plastic deformation. Fig. 7a–c depicts some examples of the killer defects found in the material. No visible differences have been detected between the population of the killer size related to HCF or LCF tests. However, a few LCF tests performed on P1 and one test from P2 showed multiple crack initiation sites on the fracture surface, as seen in Fig. 7d. It is well known that large applied strains promote multiple crack initiation, because a large driving force involves more cracks overcoming the FCG threshold. The reason why this behaviour was not noticed on P3 and is very unlikely for P2 can mainly be attributed to the lower density of large defects [9], which makes less probable the presence of multiple large defects on the same plane of the main crack.

One of the considerations to be drawn is that the artificial defects introduced in this material yield a conservative assessment of the lower bound of the data in both HCF and LCF. For this reason, the possibility of easily assessing a lower bound resistance by introducing an artificial defect in the samples appears promising to simplify, shorten and reduce the cost of material testing campaigns.

3.3. Strain localisation near defects

To assess the strain localisation near natural defects, two samples from P1 with different orientations were investigated by DIC. In the horizontal sample, preliminary CT results showed the presence of three large subsurface defects close to one another. The dimension of these defects was around 100–200 μm in terms of $\sqrt{\text{area}}$ parameter. The hysteresis cycle for the horizontal sample is shown in Fig. 8a. As indicated in the stress–strain plot, the image of the un-deformed specimen surface is defined as reference image for DIC correlation. All the images captured successively during specimen loading are defined as deformed images. The correlations between the reference and deformed images (captured after specific number of cycles) determine the strain maps. Fig. 8b indicates the dimension of the subset used for the correlation and the DIC area of interest in the extensometer region. The DIC strain maps collected at different test interruptions (Fig. 8c) characterize the development of the main crack from the early stages to the final crack length at which the test was interrupted (cycle 1588). Remarkably, strain localizations arise at the beginning of the test. At cycle 10, local perturbations of the strain field indicate crack nucleation from the manufacturing defect. Note that strain localisations in the same position was already visible at cycle one, although it was hardly distinguishable because of the noise.

A second experiment was conducted on a vertical specimen confirmed the same results, as depicted in Fig. 9. The DIC strain maps shown in the comparison were obtained by correlating the images captured at the minimum load with those captured at the maximum load of the hysteresis cycles. The arrows indicate high local strain gradients, highlighting the presence of manufacturing defects. Even in this case, the strain localization for the vertical sample suggests the onset of crack propagation already at cycle 10. These results clearly demonstrate that the nucleation time for fatigue cracks in the LCF re-gime can in first instance be considered negligible with respect to crack propagation time, in accordance with the results in [37,38].

3.4. Crack opening and closure

The determination of crack opening and closure levels are mandatory for a correct determination of the elastic–plastic driving force

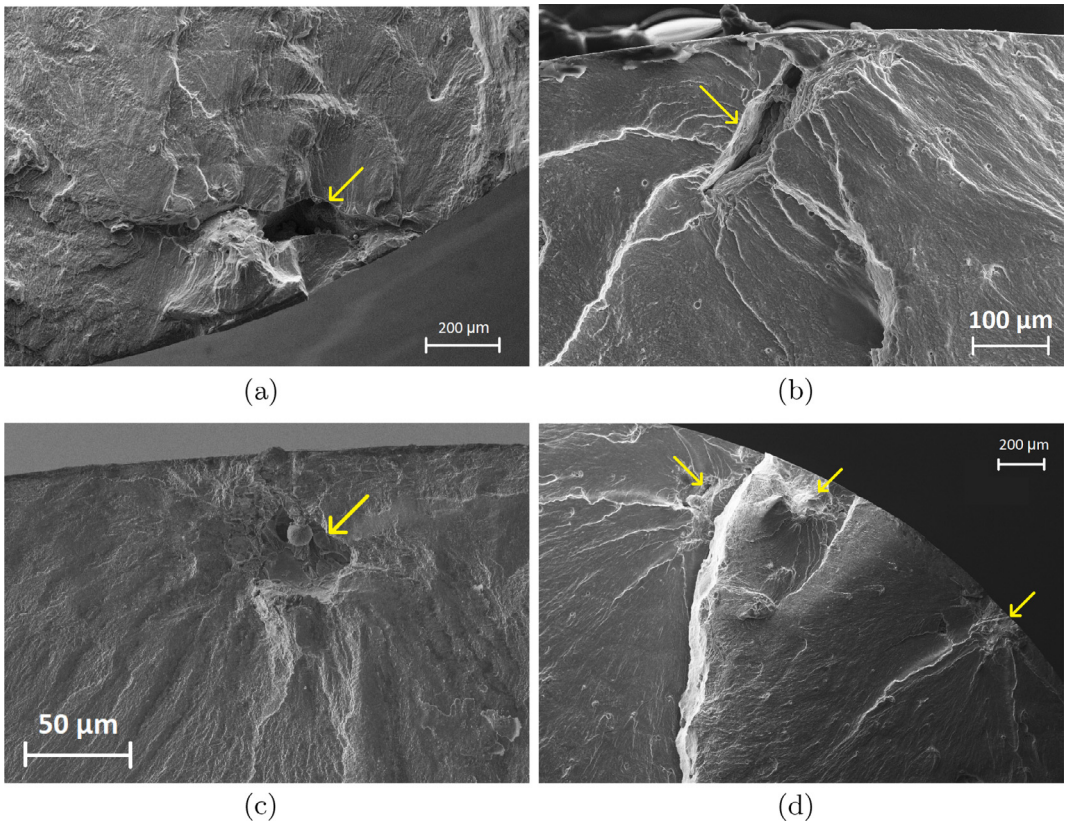

Fig. 7. Killer defects at the origin of fatigue failure in P1 (highlighted by arrows): typical finding in (a) P1; (b) P2; (c) P3; (d) case of multiple crack initiation in P1.

acting on the crack [20,54]. The most common formulation to estimate the crack opening level was defined by Newman [55,56] and is the standard assumption adopted for fatigue crack propagation simulation (e.g., NASGRO [57]). The Newman model was defined for long cracks under constant amplitude loading with plastically-deformed material in the wake of the advancing crack. This formulation is based on two main parameters: the constraint factor α and the ratio σ_{max}/σ_0, where the flow stress σ_0 is calculated as:

$$\sigma_0 = \frac{1}{2}(R_{p0.2} + R_m) \tag{2}$$

A fixed ratio $\sigma_{max}/\sigma_0 = 0.3$ is often assumed to simulate HCF life [57]. The constraint factor accounts for three-dimensional constraint effects for tensile yielding and depends on crack geometry and remote loading conditions. When the plastic zone is small compared to the material thickness, nearly plane-strain conditions are applicable. This is generally the case in the HCF regime, which is the reason why the NASGRO software considers a constant value for α for the whole pro-pagation in the elastic region. Considering aluminium, a value of $\alpha = 1.9$ is generally adopted, as is also reported in the NASGRO data-base.

In the case of large plastic zone, instead, a plane-stress condition is applicable, and conservative assessments of crack opening levels can be obtained by setting $\alpha = 1$. At the same time, one has to consider the real applied σ_{max}/σ_0 ratio, where the flow stress σ_0 is calculated as in Eq. (2), replacing the yield stress $R_{p0.2}$ with the cyclic yield stress $R_{p0.2}$ [23,54]. In the presence of plastic deformation, the stress–strain level at which crack closure occurs differs from the opening point. As a general statement, the opening stress is very low at the beginning of short crack growth and increases with crack length according to the development of the plastic wake. A saturation state is finally reached where further crack growth does not significantly alter the crack closure stress [23]. Two approaches are reported in literature to define the closure level. According to Vorwmald [23], the crack is closed when the deformation in the unloading branch of the hysteresis loop equals the opening strain (Eq. (3)), while McClung and Sehitoglu [58] proposed a different relationship (Eq. (4)).

$$\epsilon_{cl} = \epsilon_{op} \tag{3}$$

$$\sigma_{cl} = \sigma_{op} \tag{4}$$

To verify which is the most accurate approach for this material, the experimental results for opening levels were obtained measuring the crack opening displacements (COD) by DIC by means of virtual extensometers (see Section 2.6). The vertical displacement fields were obtained at six test interruptions in a LCF crack propagation test performed at strain range $\Delta\epsilon = 0.6\%$. One example of the displacement map is reported in the contour plot of Fig. 10a. The virtual extensometer technique consists in positioning a series of fictitious extensometers behind the crack tip at various distances d and correlate the resulting displacement with the remote stress. This technique has been largely adopted in the case of cracks propagating in HCF condi-tions [59–61]. More recently, it has also been adopted for LCF condi-tions [62] and multiaxial loading [63]. In Fig. 10a, the original COD versus remote stress is reported in terms of plastic COD ($COD_{pl,DIC}$). The opening stress is then defined as the point in the upward branch that differs 1.5% from the maximum $COD_{pl,DIC}$ [64]. This methodology was observed to provide robust opening stress measurements at different distances d from the crack tip. Fig. 10b summarises the experimental opening stress trend during crack advancement. As expected, the opening stress increases in the first stages of propagation and reaches a saturated value. This analysis confirms that Newman's formulation yields good estimates of the opening levels even in presence of plasticity.

Considering crack closure, it is difficult to uniquely define the correct stress level. The experimental data seem to suggest a point in the middle between Vormwald's (Eq. (3)) and McClung's (Eq. (4)) hypotheses. Being more conservative, Vormwald's hypothesis has been

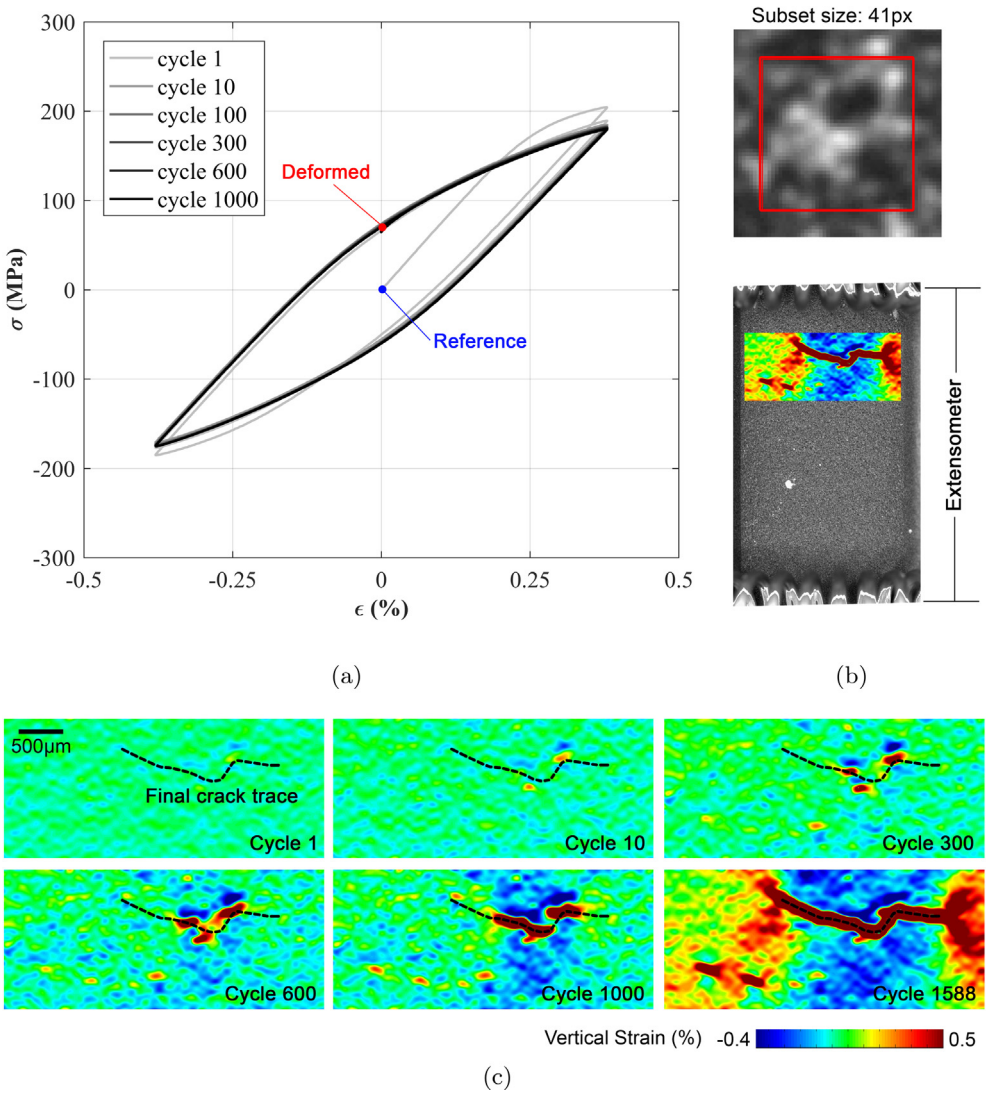

Fig. 8. Analysis of crack formation on a P1 specimen: (a) detail of the $\sigma-\epsilon$ cycle where the reference image was taken at $N = 0$; (b) details of the crack position; (c) sequence of axial strain maps related to the maximum load.

adopted for the crack propagation simulations presented in Sections 4 and 5.

4. Analysis of Low Cycle Fatigue in terms of crack propagation

Romano et Al. [9] have shown that the fatigue properties of different batches of AlSi10Mg produced by SLM can be considerably changed by slightly adjusting some process parameters and that manufacturing defects are the main reason explaining these differences. When the material is deformed in the elastic field, the dimension of the critical defect in a given volume of material can be estimated by measuring the defect distribution through CT scanning and applying statistics of extremes to determine the maximum defect size in the surface volume [18]. Considering that the time spent for crack nucleation can be considered negligible with respect to crack propagation, a FCG model can be adopted for HCF estimate. To extend the FCG model to the LCF regime, this assumption was herein confirmed by means of DIC strain measurements, demonstrating that strain localisa-tion in correspondence of natural defects starts in the very first fatigue cycles (see Section 2.6).

The goal of the present section is to extend the crack propagation model to perform LCF life estimates. This can be achieved through the definition of a model that properly considers the elastic–plastic driving force.

4.1. Fatigue crack growth model

In Section 3.4, it was shown that a good approximation of the experimental results can be obtained by adopting the Newman's formulation to model crack opening and the Vormwald's hypothesis for crack closure. To define a univocal formulation for the crack opening and closing levels in both HCF and LCF conditions, some hypotheses on the Newman's model parameters are discussed in the following. Based on the experiments described in Section 3.4, the model presented adopts a fixed constraint factor for plane-strain condition of $\alpha = 1.9$ in the whole range of applied stresses. This choice allows crack closure to be described in both the HCF and LCF crack propagation regimes, with a slight and conservative difference in the intermediate region. At the same time, the constant value of $\sigma_{max}/\sigma_0 = 0.3$ typically adopted for the NASGRO equation is a good approximation for low applied stress levels, but it gives non-conservative results at larger stress levels. A more precise description can be obtained adopting the real applied σ_{max}/σ_0, defining σ_0 in cyclic plasticity as in Section 3.4. Summarising, the model assumes a constant $\alpha = 1.9$ and the real applied σ_{max}/σ_0. These

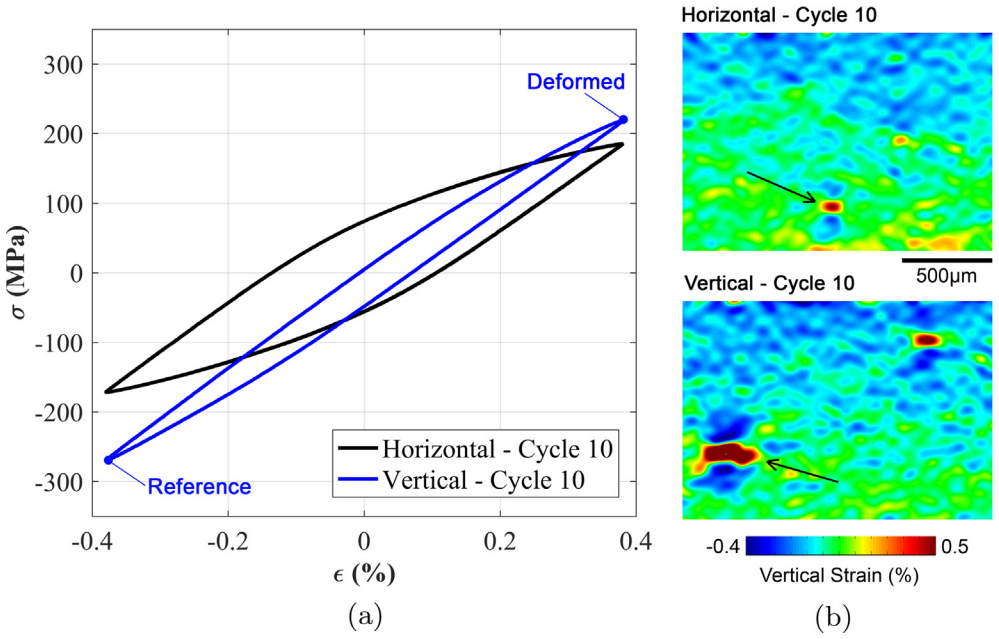

Fig. 9. Comparison between the LCF behaviour after the first 10 cycles for horizontal and vertical orientations under a strain range of $\Delta\epsilon = 0.76\%$: (a) the hysteresis loops indicate a strong influence of the sample orientation; (b) the DIC strain maps highlight the presence of local strain inhomogeneities, as a clear indication of early crack nucleation around the manufacturing defects.

assumptions give a correct estimation for both elastic and plastic conditions and a slightly conservative result in the middle region.

To properly model the fatigue strength for a defected material, one has to consider the adoption of a proper fracture parameter that considers both the elastic and plastic material behaviours. In fact, above one third of the endurance limit in the absence of defects, $1/3{\cdot}\Delta\sigma_{w0}$, the driving force should be calculated considering plasticity at the crack tip [65]. In particular, in the LCF regime it has been shown [23,58,66] that the crack growth rate and life prediction can be precisely obtained by integrating the equation:

$$\frac{da}{dN} = f(\Delta J_{\text{eff}}) \tag{5}$$

where the $f(\Delta J_{\text{eff}})$ curve is the $da/dN{-}\Delta K_{\text{eff}}$ curve expressed in terms of ΔJ_{eff} . The fatigue crack propagation law adopted is a NASGRO-type equation (Eq. (6)), which does not consider the instability developing when approaching the material's fracture toughness.

$$\frac{da}{dN} = C{\cdot}\Delta K_{\text{eff}}^{n}\left(1{-}\frac{\Delta K_{\text{th,eff}}}{\Delta K_{\text{eff}}}\right)^{p} \tag{6}$$

The parameters C, n, p have been fitted on the experimental data depicted in Fig. 11. The calculation of ΔJ_{eff} from FCG data can be performed adopting Eq. (7), where $E' = \frac{E}{(1-\nu^2)}$ is the Young's modulus for plane strain condition and ν is the Poisson's ratio.

$$\Delta J_{\text{eff}} = \frac{\Delta K_{\text{eff}}^{2}}{E'} \tag{7}$$

In this way, the crack growth rate is obtained as a function of ΔJ_{eff} from the typical crack propagation tests ($\Delta K_{\text{eff}}{-}da/dN$ curve), Fig. 11. The adoption of ΔJ instead of ΔK allows to uniquely describe the crack driving force in both LEFM and EPFM.

4.2. Modelling of elastic–plastic driving force

Under LCF conditions, the values of ΔJ_{eff} can be calculated with the formulation by Rabbolini et al. [67]. A crack length independent parameter P_J [20] is introduced as in Eq. (8):

$$\Delta J_{\text{eff}} = Y^{2}{\cdot}a{\cdot}P_{J,\text{eff}} \tag{8}$$

where Y is the boundary correction factor for SIF calculation and a is the crack length. The term $P_{J,\text{eff}}$ is defined by Eq. (9).

$$P_{J,\text{eff}} = \pi\left(\frac{\Delta\sigma_{\text{eff}}^{2}}{E'} + \frac{3}{4{\cdot}\sqrt{n'}}\Delta\sigma_{\text{eff}}{\cdot}\Delta\,\epsilon_{\text{pl,eff}}\right) \tag{9}$$

The effective stress range $\Delta\sigma_{\text{eff}}$ and effective plastic strain range $\Delta\,\epsilon_{\text{pl,eff}}$ are calculated according to Eqs. (10) and (11). This is achieved defining the opening and closing levels (see Section 3.4) and the corresponding points on the stabilised hysteresis curve based on the Ramberg–Osgood model (see Section 3.1).

$$\Delta\sigma_{\text{eff}} = \sigma_{\max}{-}\sigma_{\text{cl}} \tag{10}$$

$$\Delta\,\epsilon_{\text{pl,eff}} = \epsilon_{\max}{-}\epsilon_{\text{op}}{-}\frac{\Delta\sigma_{\text{eff}}}{E} \tag{11}$$

To summarize, knowing the stabilised cyclic response and the crack closure levels, the value ΔJ_{eff} can easily be calculated for any cyclic stress or strain applied to the material and the life predictions can be performed integrating Eq. (5).

At this point, it is important to verify the ability of the model to properly determine the growth rate of fatigue cracks subjected, for example, to LCF at $R_\epsilon = -1$. In Section 2.6, it has been introduced that the growth rates of fatigue cracks growing from artificial defects in specimens tested in LCF at $R_\epsilon = -1$ have been measured by DIC, optical microscopy and replica techniques for P1 and P2. Therefore, the model has been applied to calculate the ΔJ_{eff} in correspondence of all the experimental crack growth rates measured. Fig. 11 confirms the quality of the assessment for both P1 and P2, as the *shifted* FCG rates are compliant with the effective FCG curve based on LEFM.

4.3. Verification on artificial defects

The model has been validated by simulating the experiments conducted on the micro-notched specimens where the crack nucleation and propagation from the artificial defects were monitored. Due to the elongated shape of the defects inside P1 (depicted in Fig. 12a), the fatigue crack propagation simulation was performed on both the depth and surface points of the crack [35]. Considering P2 and P3, instead, the nearly semi-circular shape of the artificial defects for FCG

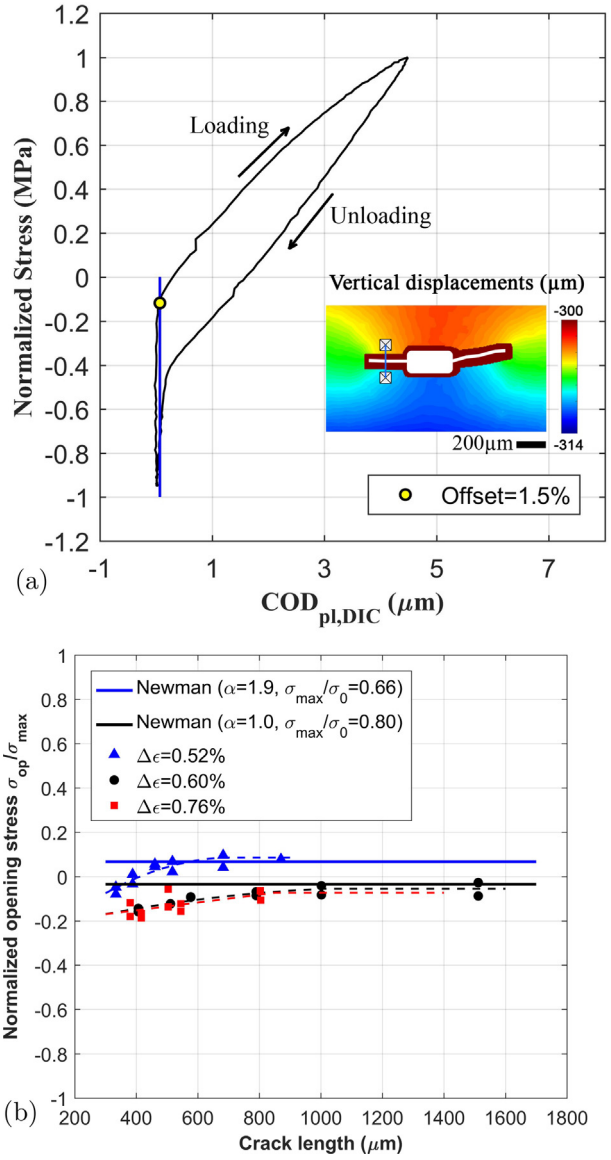

Fig. 10. Results of crack closure measurements on P2 specimens: (a) the COD is calculated from the DIC displacement maps using the virtual extensometer reading and the opening stress is determined according an offset of 1.5% from the linear elastic line (see the text for more details); (b) comparison with Newman's model.

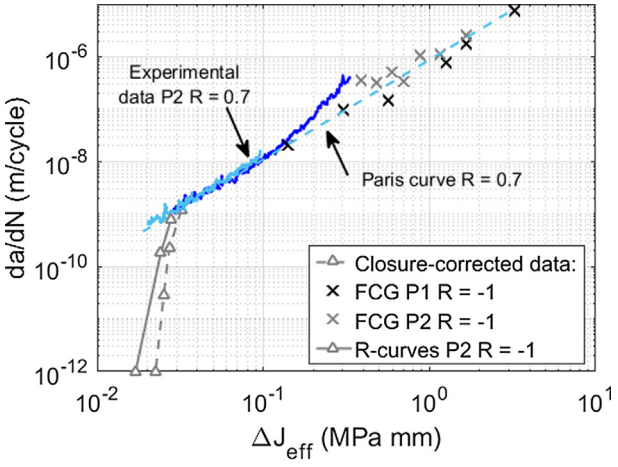

Fig. 11. Fatigue crack growth tests performed on P1 and P2.

simulations at a fixed shape ratio of $a/c = 1$ (see Fig. 12b). The comparison of the two simulation approaches on P1 showed limited difference in terms of life (below 5%). Therefore, the problem has been simplified simulating only semi-circular cracks. The stabilised cyclic curve of each specimen has been adopted for the calculation of ΔJ_{eff}.

The predicted number of cycles to failure correlates very well with the experimental results in all the strain ranges investigated, as depicted in Fig. 12c. The error committed by the simulations stays within a factor 2 with regards to the number of cycles to failure N_f, which is a common result for FCG simulations [22]. The lower precision over the knee-point of the S-N curve (i.e., $2{\cdot}10^5$ cycles) is due to the other sources of scatter (e.g., microstructure, residual stresses, anisotropy), which become more important when the fatigue curve tends to flatten.

4.4. Life predictions for natural defects

In this section, the model is applied to perform HCF and LCF life predictions in the presence of natural defects for the three processes investigated. To perform the life predictions, the model requires the following input data:

1. the cyclic curve;
2. the FCG curve and crack propagation threshold in absence of crack closure (effective curve herein determined at load ratio $R = 0.7$);
3. the CT scan of a volume of material to estimate the prospective maximum size of the defect.

The unique source of scatter introduced in the simulations is the initial defect size, which is determined from the CT data as a percentile of the maximum defect distribution in the surface gauge volume [9,18]. As the vast majority of failures was originated by surface defects, the boundary correction factor for SIF calculation Y is defined according to the standard solution for a surface crack propagating in a rod [68], the crack size being described only by its depth a_i, while crack shape is assumed to be semi-circular.

The results are depicted in Fig. 13a–c. A 95% scatter band has been obtained by considering the propagation of the 2.5% and 97.5% percentiles of the initial crack size. The latter estimate refers to a dimension similar to that of the artificial defects; therefore, a direct comparison is possible. The picture shows that the model is able to estimate both the average life and the scatter in the whole range of strains and stresses investigated during the LCF and HCF test campaigns. A slight overestimation of the life is obtained for some of the samples of P3 and for the artificial defects. This could be due to the lack of data regarding the crack propagation curve for this process, especially considering that the microstructure can have an important influence on the FCG of such small cracks. Moreover, in the presence of very small defect sizes, as in this case, the variability in the fatigue life due to the defects is limited, and other sources of scatter can become non-negligible and require further investigation. Overall, considering the fatigue limit region, all the estimates yield good results.

Fig. 13b reports the HCF assessment obtained by introducing a residual stress for P2. The presence of residual stresses does not change the hysteresis loop, but it influences the stress ratio and the driving force acting on the crack by shifting the crack opening stress through the R and σ_{max}/σ_0 parameters of the Newman's model. A stress of 50 MPa was obtained by averaging the measurements reported in Sec-tion 2.3. The FCG simulations show that the expected life does not sensibly change for the material and condition investigated. In general, considering the residual stresses can provide a more robust and conservative assessment in HCF. Such an effect was not considered for $\Delta\epsilon > 0.4\%$ because of the mean stress relaxation in the LCF regime. As no residual stress measurements were available, these simulations were not carried out for P1 and P3.

It is important to remark that the ability of the model to estimate the experimental scatter is due to a correct estimation of the critical defect

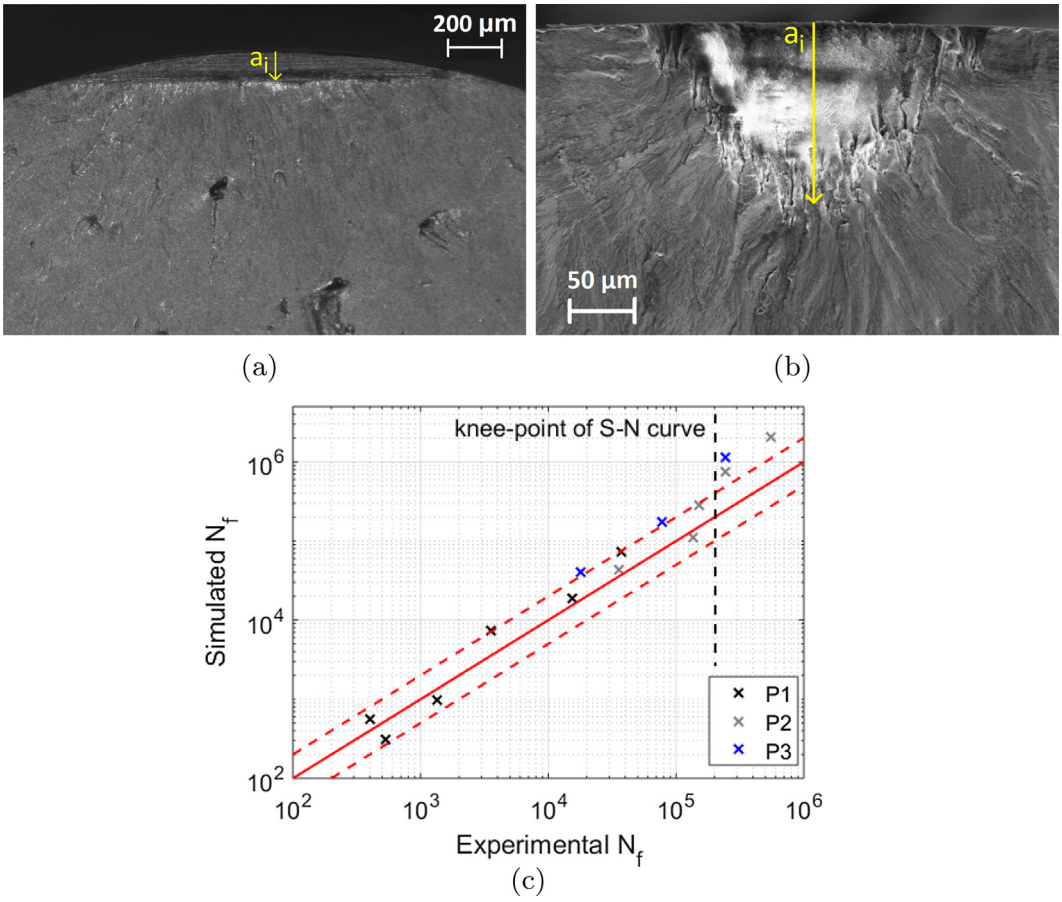

Fig. 12. Validation of LCF life prediction model simulating the propagation of artificial defects: initial crack depth definition for (a) P1 and (b) P2-P3; (c) experimental vs simulated fatigue life.

size. Experimental investigations on AlSi10Mg [9] and Ti-6Al-4V [17] alloys have demonstrated that defect size plays a fundamental role both close to the fatigue limit and in the short-life regions. Moreover, it has been shown that the Kitagawa diagram can be adopted even for finite life assessment, as the ratio $\Delta\sigma/\Delta\sigma_w$ is independent of the critical defect size. Based on this consideration, in Section 5 are presented Kitagawa-like defect acceptance maps valid for both the fatigue limit and finite life regions.

5. Discussion

In this work, a FCG model based on the elastic–plastic parameter ΔJ_{eff} has been presented, which is capable of predicting the life of smooth and micro-notched specimens of the AlSi10Mg alloy produced by SLM both in the HCF and LCF regimes, provided that all the relevant material data are available. The model uses limited input material data, the cyclic curve and the effective crack growth curve. In addition, it requires a CT scan of a volume of material to characterize the defect distribution for a particular manufacturing process. Details on the verification of the hypothesis of the model were given in the previous sections. In particular, classical FCG experiments were corroborated with DIC measurements demonstrating that the fatigue life of the additively manufactured AlSi10Mg alloy can be described purely by a crack growth model, as the crack incubation time is negligible with respect to the propagation time. The crack opening model assumed was also verified with crack closure measurements performed by means of the DIC virtual extensometer technique.

The applicability of the model can be further extended to define design maps where the allowable stress is calculated based on the defect dimension and the desired component life. In the following, the fatigue crack propagation model has been used to assess the relationship between defect size, fatigue life and applied stress. This is achieved defining the Kitagawa diagram and extending this concept to finite lives, in order to consider the whole range of applicable stresses and strains.

The adoption of the Kitagawa diagram to AM materials has been already verified in [14]. The classical way to obtain the diagram, for a given material, is to perform tests with micronotches of different size [16,69]. However, the main drawback of this method is the large experimental effort required in terms of time and number of specimens involved.

Alternatively, the ΔJ_{eff} FGC model could be applied to the threshold condition, as suggested in [70]. According to this concept, the non-propagation condition for a short crack with a size a can be calculated as:

$$\Delta\sigma_w = \Delta\sigma: \Delta J_{\text{eff}}(a, \Delta\sigma) = \Delta K^2_{\text{th,eff}} \cdot E' \tag{12}$$

This method has been verified considering the experimental data available for P2. As reported in Section 2.5, the resistance curve tests have highlighted a fatigue crack propagation threshold at $R = -1$ of 3.2–3.6 MPa$\sqrt{\text{m}}$, corresponding to an effective threshold of almost 1.20–1.35 MPa$\sqrt{\text{m}}$.

The estimated Kitagawa obtained with this $\Delta K_{\text{th,eff}}$ is depicted in Fig. 14a and compared with the experimental results [9]. The figure confirms very good agreement between the experimental data and the proposed estimates. A slight difference between the El-Haddad model and the estimation based on ΔJ_{eff} is visible for the fatigue limit in the absence of defects. A precise definition of this region is not important for the current material, as the defect size is always larger. However, it could be important for material subjected to hot isostatic pressing.

The same considerations can be drawn for P1 and P3. No threshold

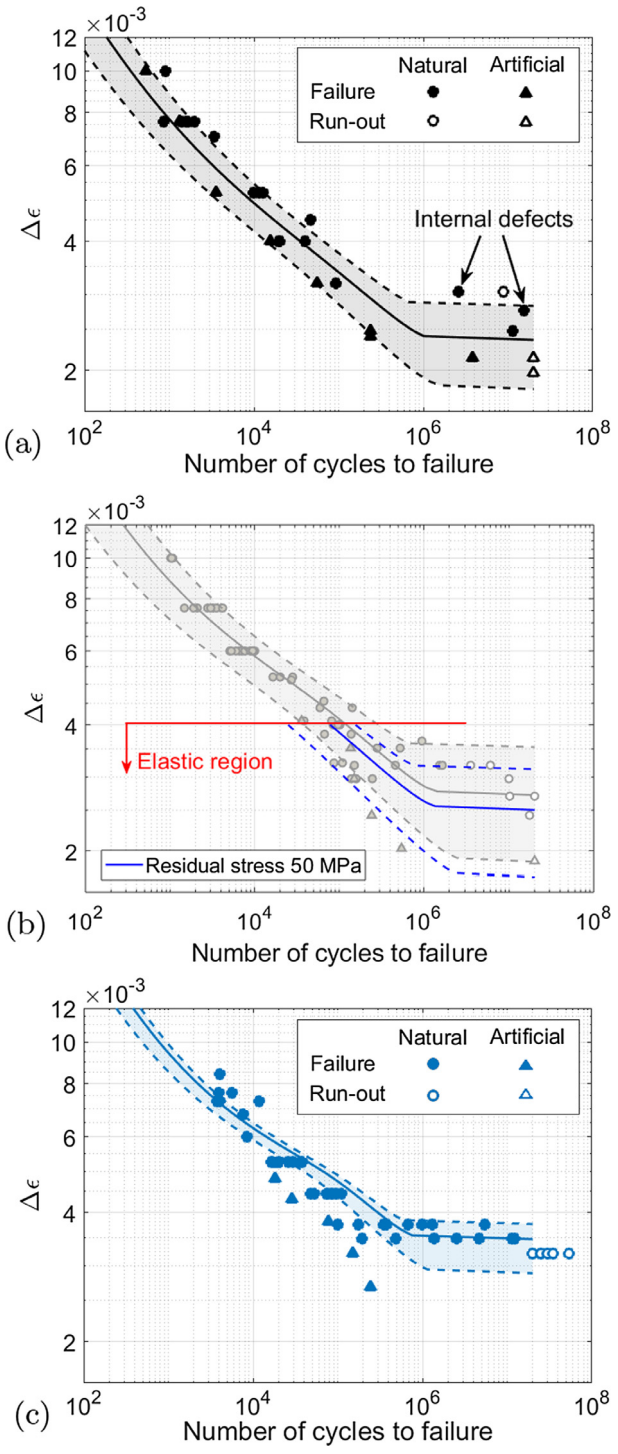

Fig. 13. Life estimates obtained using the proposed elastic–plastic FCG model: (a) P1; (b) P2; (c) P3.

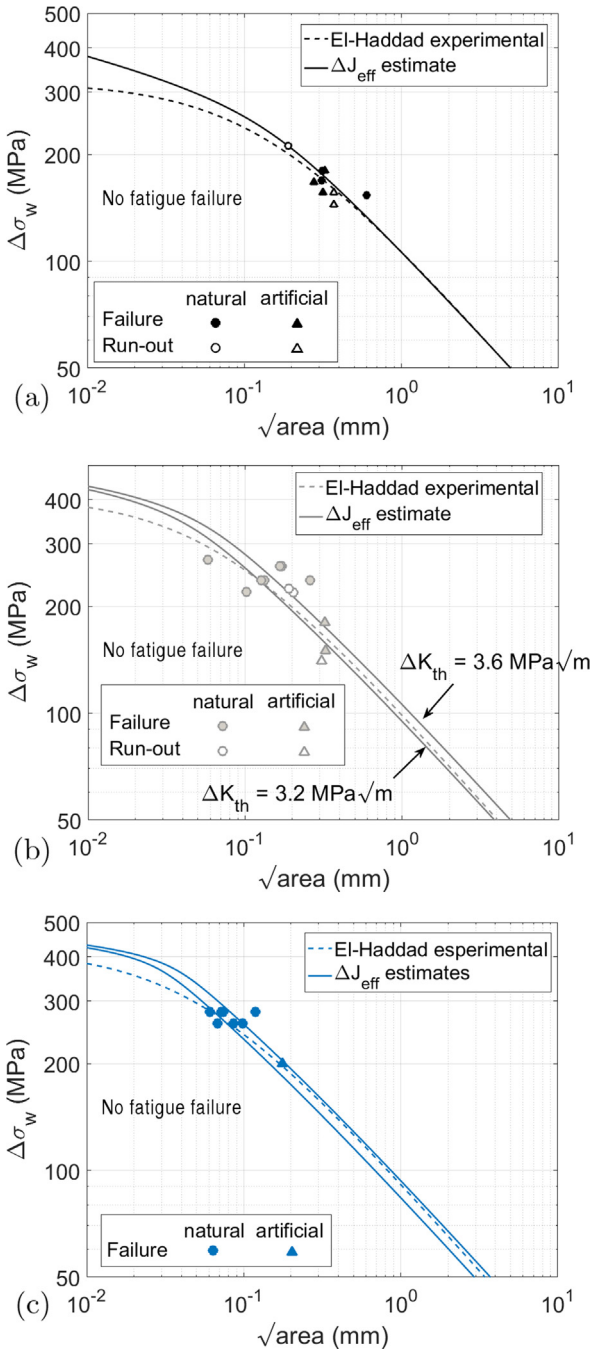

Fig. 14. Experimental Kitagawa diagram [9] (El-Haddad formulation) and estimate performed adopting ΔJ_{eff}: (a) P2; (b) P1; (c) P3. No fatigue failure is expected below the curve.

data are available for these materials, but the estimates based on fatigue tests suggest a ΔK_{th} at $R = -1$ of approximately 4.1 MPa$\sqrt{\text{m}}$ for P1 (see Fig. 14b). Finally, the threshold value estimated for P3 is consistent with the one of P2.

Summarising, a good estimate of the average Kitagawa diagram can be obtained knowing the crack propagation threshold in the absence of crack closure ($R = 0.7$) and (when the defect size is very small) the cyclic curve of the material. For a robust probabilistic assessment, the determination of the intrinsic scatter associated to this diagram should also be obtained. The experimental data available for this material have highlighted a variability of approximately 10%, due to several sources of scatter (e.g., microstructure, residual stresses, anisotropy, errors during the testing and measuring phases) [9].

The propagation model has been evaluated in a large range of applied stresses and critical defect sizes to draw a map of the estimated fatigue life similar to that reported in [71]. The results obtained for P2 have been interpolated and the importance of the defect size is clearly shown by the iso-life lines depicted in Fig. 15a. The importance of defect size on fatigue life is clearly depicted in Fig. 15b for several applied stresses. Having almost the same cyclic curves and FCG properties, the life estimates obtained for P3 are described by the same diagram. Finally, the colormap highlights the agreement between these estimates and the experimental data from P2 and P3. Of course, there

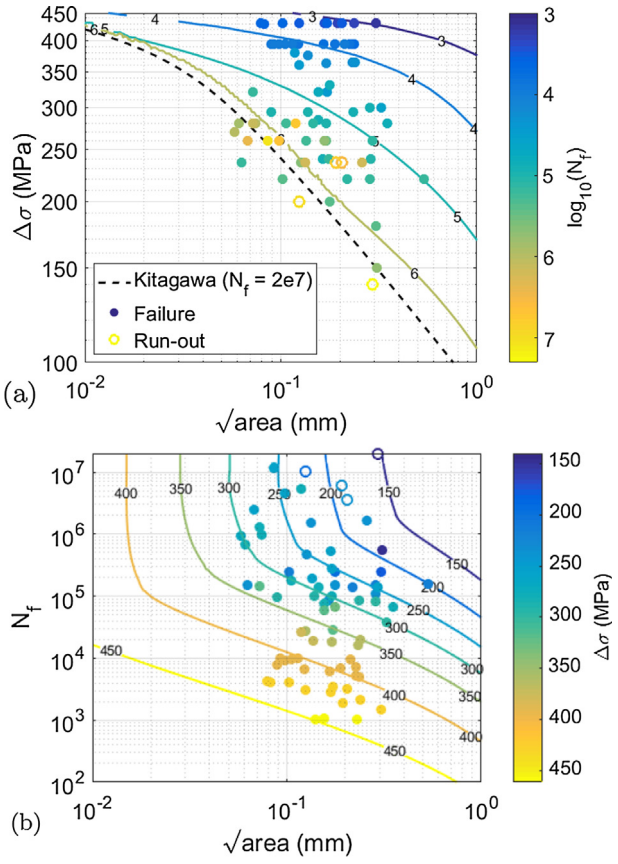

Fig. 15. Fatigue resistance estimated with the FCG model for P2 and P3 and comparison with the experimental results: (a) iso-life lines as a function of applied stress and defect size; (b) iso-stress lines as a function of fatigue life and defect size.

are several other sources of variability besides the initial crack size (e.g., anisotropy, residual stresses, microstructure), therefore, some limited error shall always be expected. This error can play an important role when dealing with probabilistic fatigue life assessments, therefore its magnitude is an important input for more sophisticated probabilistic analyses (e.g., [72,73]).

6. Conclusions

This study has summarised the tests and modelling performed on the Aluminium alloy AlSi10Mg produced by SLM by three different processes. The significant results of the activity are:

- the defect size is the principal cause of variability in the fatigue resistance of the material, even in LCF. A safe fatigue life assessment can be determined introducing artificial defects having a dimension dependent on the defect population;
- the cyclic yield strength of the material can change among different processes and can be influenced by other factors even inside the same build (e.g., anisotropy and residual stresses);
- plasticity plays an important role for the determination of the fatigue resistance of AM parts; therefore, simple crack propagation simulations in the fully-elastic regimes (e.g., standard NASGRO simulations) can yield non-conservative results;
- a good estimate of average life and scatter can be obtained with a limited amount of input data (i.e., defect distribution, stabilised cyclic curve and FCG curve, including the crack propagation threshold) by adopting a fatigue crack growth model based on ΔJ_{eff} concepts.
- the proposed model can be adopted to assess the influence of manufacturing defects on LCF and HCF resistance of AM parts and to estimate the Kitagawa diagram. This defect-tolerant safe life assessment can simplify and enhance the design and verification phases.

All the investigations performed have highlighted the important influence that manufacturing defects cover on the fatigue resistance of AM parts, as well as the main variables needed for a proper fatigue assessment. This demonstrates the importance of the application of probabilistic defect-tolerant models for the fatigue assessment of complex parts inside a Finite Element framework. This kind of software has been developed by PoliMi [73] and will be validated in appropriate case studies.

Acknowledgements

The activity of S. Romano has been supported by ESA through the Networking Partnering Initiative (NPI). We acknowledge J. Gumpinger (ESA/ESTEC) and T. Ghidini (ESA/ESTEC) for permission to publish results of the test data for P3 specimens, that were carried out at ESA. We also acknowledge the support of RUAG, in particular M. Gschweitl, for manufacturing the specimens and for permission to publish the results of this research activity.

Contributions to the paper are: (i) S. Romano performed the tests together with modelling and analyses and he took care of the manuscript preparation; (ii) L. Patriarca took care of all the experiments and data analysis related to DIC and contributed to the manuscript; (iii) S. Foletti helped with the cyclic and ΔJ_{eff} modelling; (iv) S. Beretta directed this research on defect-based analysis and contributed to the manuscript.

References

[1] Zhai Y, Lados DA, LaGoy JL. Additive manufacturing: Making imagination the major limitation. JOM 2014;66(5):808–16. https://doi.org/10.1007/s11837-014-0886-2.
[2] Huang R, Riddle M, Graziano D, Warren J, Das S, Nimbalkar S, et al. Energy and emissions saving potential of additive manufacturing: the case of lightweight aircraft components. J Clean Prod 2016;135:1559–70. https://doi.org/10.1016/j.jclepro.2015.04.109.
[3] Orme ME, Gschweitl M, Ferrari M, Vernon R, Madera IJ, Yancey R, et al. Additive manufacturing of lightweight, optimized, metallic components suitable for space flight. J Spacecraft Rockets 2017;54(5):1–10. https://doi.org/10.2514/1.A33749.
[4] Persenot T, Buffière J-Y, Maire E, Dendievel R, Martin G. Fatigue properties of EBM as-built and chemically etched thin parts. Proc Struct Integr 2017;7:158–65. https://doi.org/10.1016/j.prostr.2017.11.073.
[5] Brandão AD, Gumpinger J, Gschweitl M, Seyfert C, Hofbauer P, Ghidini T. Fatigue properties of additively manufactured AlSi10Mg - surface treatment effect. Proc Struct Integ 2017;7:58–66. https://doi.org/10.1016/j.prostr.2017.11.061.
[6] Mohammad A, Mohammed MK, Alahmari AM. Effect of laser ablation parameters on surface improvement of electron beam melted parts. Int J Adv Manuf Technol 2016;87(1):1033–44. https://doi.org/10.1007/s00170-016-8533-4.
[7] Król M, Dobrzański LA, Reimann L, Czaja I. Surface quality in selective laser melting of metal powders. Arch Mater Sci 2013;60(2):87–92.
[8] Klingvall Ek R, Rännar L-E, Bäckström M, Carlsson P. The effect of EBM process parameters upon surface roughness. Rapid Prototyp J 2016;22(3):495–503. https://doi.org/10.1108/RPJ-10-2013-0102.
[9] Romano S, Brückner-Foit A, Brandão AD, Gumpinger J, Ghidini T, Beretta S. Fatigue properties of AlSi10Mg obtained by additive manufacturing: Defect-based modelling and prediction of fatigue strength, Eng Fract Mech. https://doi.org/10.1016/j.engfracmech.2017.11.002.
[10] Gorelik M. Additive manufacturing in the context of structural integrity. Int J Fatigue 2017;94:168–77. https://doi.org/10.1016/j.ijfatigue.2016.07.005.
[11] Seifi M, Salem A, Beuth J, Harrysson O, Lewandowski JJ. Overview of materials qualification needs for metal additive manufacturing. Jom 2016;68(3):747–64. https://doi.org/10.1007/s11837-015-1810-0.
[12] Seifi M, Salem A, Satko D, Shaffer J, Lewandowski JJ. Defect distribution and microstructure heterogeneity effects on fracture resistance and fatigue behavior of EBM Ti-6Al-4V. Int J Fatigue 2017;94:263–87. https://doi.org/10.1016/j.ijfatigue.2016.06.001.
[13] Peralta AD, Enright M, Megahed M, Gong J, Roybal M, Craig J. Towards rapid qualification of powder-bed laser additively manufactured parts. Integr Mater Manuf Innov 2016;5(1):1–23. https://doi.org/10.1186/s40192-016-0052-5.
[14] Beretta S, Romano S. A comparison of fatigue strength sensitivity to defects for materials manufactured by AM or traditional processes. Int J Fatigue 2017;94:178–91 Special issue on Additive Manufacturing.
[15] Kitagawa H, Takahashi S. Applicability of fracture mechanics to very small cracks

or the cracks in the early stage. In: Proc 2nd Int Conf Mech Behaviour of Materials - ICM2; 1976. p. 627–631.
[16] Murakami Y. Metal fatigue: effects of small defects and nonmetallic inclusions. Oxford: Elsevier; 2002.
[17] Tammas-Williams S, Withers PJ, Todd I, Prangnell PB. The influence of porosity on fatigue crack initiation in additively manufactured titanium components. Sci Rep 2017;7(1):1–13. https://doi.org/10.1038/s41598-017-06504-5.
[18] Romano S, Brandão AD, Gumpinger J, Gschweitl M, Beretta S. Qualification of AM parts: extreme value statistics applied to tomographic measurements. Mater Des 2017:1–34.
[19] Chell GG, McClung RC, Kuhlman CJ, Russell DA, Garr K, Donnelly B. Guidelines for proof test analysis. Tech Rep, NASA; 1999.
[20] Vormwald M. Elastic-plastic fatigue crack growth. Adv methods fatigue assess. Berlin Heidelberg: Springer; 2013. p. 391–481.
[21] Miner M. Cumulative damage in fatigue. ASME conference of the aviation division; 1945. p. 159–64.
[22] Heuler P, Schuetz W. Assessment of concepts for fatigue crack initiation and propagation life prediction. Materialwiss Werkstofftech 1986;17(11):397–405. https://doi.org/10.1002/mawe.19860171105.
[23] Vormwald M, Seeger T. The consequences of short crack closure on fatigue crack growth under variable amplitude loading. Fatigue Fracture Eng Mater Struct 1991;14(2/3):205–25.
[24] Hertel O, Vormwald M. Short-crack-growth-based fatigue assessment of notched components under multiaxial variable amplitude loading. Eng Fract Mech 2011;78(8):1614–27.
[25] Noroozi A, Glinka G, Lambert S. A two parameter driving force for fatigue crack growth analysis. Int J Fatigue 2005;27(10-12):1277–96.
[26] Noroozi A, Glinka G, Lambert S. A study of the stress ratio effects on fatigue crack growth using the unified two-parameter fatigue crack growth driving force. Int J Fatigue 2007;29(9-11):1616–33.
[27] Bentachfine S, Pluvinage G, Gilgert J, Azari Z, Bouami D. Notch effect in low cycle fatigue. Int J Fatigue 1999;21:421–30. https://doi.org/10.1016/S0142-1123(99)00004-3.
[28] Agius D, Kourousis KI, Wallbrink C, Song T. Cyclic plasticity and microstructure of as-built SLM Ti-6Al-4V: The effect of build orientation. Mater Sci Eng, A 2017;701(June):85–100. https://doi.org/10.1016/j.msea.2017.06.069.
[29] Benedetti M, Fontanari V, Bandini M, Zanini F, Carmignato S. Low- and high-cycle fatigue resistance of Ti-6Al-4V ELI additively manufactured via selective laser melting: Mean stress and defect sensitivity. Int J Fatigue 2018;107(August 2017):96–109. https://doi.org/10.1016/j.ijfatigue.2017.10.021.
[30] Fatemi A, Molaei R, Sharifimehr S, Phan N, Shamsaei N. Multiaxial fatigue behavior of wrought and additive manufactured ti-6al-4v including surface finish effect. Int J Fatigue 2017;100:347–66.
[31] Li Z, Tian XJ, Tang HB, Wang HM. Low cycle fatigue behavior of laser melting deposited TC18 titanium alloy. Trans Nonferrous Met Soc China (English Edition) 2013;23(9):2591–7. https://doi.org/10.1016/S1003-6326(13)62772-7.
[32] Xue Y, Pascu A, Horstemeyer MF, Wang L, Wang PT. Microporosity effects on cyclic plasticity and fatigue of LENS-processed steel. Acta Mater 2010;58(11):4029–38. https://doi.org/10.1016/j.actamat.2010.03.014.
[33] Aydinöz ME, Brenne F, Schaper M, Schaak C, Tillmann W, Nellesen J, et al. On the microstructural and mechanical properties of post-treated additively manufactured Inconel 718 superalloy under quasi-static and cyclic loading. Mater Sci Eng: A 2016;669:246–58. https://doi.org/10.1016/j.msea.2016.05.089.
[34] Kirka MM, Greeley DA, Hawkins C, Dehoff RR. Effect of anisotropy and texture on the low cycle fatigue behavior of Inconel 718 processed via electron beam melting. Int J Fatigue 2017;105:235–43. https://doi.org/10.1016/j.ijfatigue.2017.08.021.
[35] Romano S, Beretta S, Foletti S. LCF response of AlSi10Mg obtained by additive manufacturing. In: Eighth international conference on low cycle fatigue (LCF8), Dresden; 2017.
[36] Sterling AJ, Torries B, Shamsaei N, Thompson SM, Seely DW. Fatigue behavior and failure mechanisms of direct laser deposited Ti-6Al-4V. Mater Sci Eng, A 2016;655:100–12. https://doi.org/10.1016/j.msea.2015.12.026.
[37] Shamsaei N, Yadollahi A, Bian L, Thompson SM. An overview of Direct Laser Deposition for additive manufacturing; Part II: Mechanical behavior, process parameter optimization and control. Additive Manuf 2015;8:12–35. https://doi.org/10.1016/j.addma.2015.07.002.
[38] Buffière JY, Savelli S, Jouneau PH, Maire E, Fougères R. Experimental study of porosity and its relation to fatigue mechanisms of model Al-Si7-Mg0.3 cast Al alloys. Mater Sci Eng A 2001;316(1-2):115–26. https://doi.org/10.1016/S0921-5093(01)01225-4.
[39] Serrano-Munoz I, Buffière J-Y, Mokso R, Verdu C, Nadot Y. Location, location & size: defects close to surfaces dominate fatigue crack initiation. Sci Rep 2017;7:1–9. 45239.
[40] Thijs L, Kempen K, Kruth JP, Van Humbeeck J. Fine-structured aluminium products with controllable texture by selective laser melting of pre-alloyed AlSi10Mg powder. Acta Mater 2013;61(5):1809–19. https://doi.org/10.1016/j.actamat.2012.11.052.
[41] Chen B, Moon SK, Yao X, Bi G, Shen J, Umeda J, et al. Strength and strain hardening of a selective laser melted AlSi10Mg alloy. Scripta Mater 2017;141:45–9. https://doi.org/10.1016/j.scriptamat.2017.07.025.
[42] Masoomi M, Pegues J, Thompson SM, Shamsaei N. A numerical and experimental investigation of convective heat transfer during laser-powder bed fusion. Accepted Addit Manuf https://doi.org/10.1016/j.addma.2018.06.021.
[43] Bagherifard S, Beretta N, Monti S, Riccio M, Bandini M, Guagliano M. On the fatigue strength enhancement of additive manufactured AlSi10Mg parts by mechanical and thermal post-processing. Mater Des 2018;145:28–41. https://doi.org/10.1016/j.matdes.2018.02.055.
[44] ASTM E606. Standard test method for strain-controlled fatigue testing; 2004. https://doi.org/10.1520/E0606-04E01.Copyright.
[45] Siddique S, Imran M, Rauer M, Kaloudis M, Wycisk E, Emmelmann C, et al. Computed tomography for characterization of fatigue performance of selective laser melted parts. Mater Des 2015;83:661–9. https://doi.org/10.1016/j.matdes.2015.06.063.
[46] Wycisk E, Emmelmann C, Siddique S, Walther F. High Cycle Fatigue (HCF) performance of Ti-6Al-4V alloy processed by selective laser melting. Adv Mater Res 2013;816-817(September 2013):134–9. https://doi.org/10.4028/www.scientific.net/AMR.816-817.134.
[47] Yadollahi A, Shamsaei N. Additive manufacturing of fatigue resistant materials: challenges and opportunities. Int J Fatigue 2017;98(January):14–31. https://doi.org/10.1016/j.ijfatigue.2017.01.001.
[48] Bode B, Wessel W, Brueckner-Foit A, Mildner J, Wollenhaupt M, Baumert T. Local deformation at micro-notches and crack initiation in an intermetallic γ-TiAl-alloy. Fatigue Fract Eng Mater Struct 2016;39(2):227–37. https://doi.org/10.1111/ffe.12356.
[49] Tanaka K, Akiniwa Y. Resistance-curve method for predicting propagation threshold of short fatigue cracks at notches. Eng Fract Mech 1988;30(6):863–76. https://doi.org/10.1016/0013-7944(88)90146-4. URL http://linkinghub.elsevier.com/retrieve/pii/0013794488901464 .
[50] Pippan R, Berger M, Stüwe HP. The influence of crack length on fatigue Crack Growth in Deep Sharp Notches. Metall Trans A 1987;18(4):429–35. https://doi.org/10.1007/BF02648804. URL http://link.springer.com/10.1007/BF02648804 .
[51] Ramberg W, Osgood WR. Description of stress-strain curves by three parameters. Tech Rep, national advisory committee for aeronautics, Washington, DC, United States; 1943.
[52] Coffin Jr. LF. A study of the effects of cyclic thermal stresses on a ductile metal. Trans ASME 1954;76:931–50.
[53] Manson SS. Behavior of materials under conditions of thermal stress. Tech Rep, national advisory committee for aeronautics; 1954.
[54] McClung RC, Sehitoglu H. Closure behavior of small cracks under high strain fatigue histories. Tech Rep; 1988.
[55] Newman JCJ. A crack-closure model for predicting fatigue crack growth under aircraft spectrum loading. Methods and models for predicting fatigue crack growth under random loading, vol. 748; 1981. pp. 53–84. https://doi.org/10.1520/STP28334S.
[56] Newman JCJ. A crack opening stress equation for fatigue crack growth. Int J Fracture 1984;24(4).
[57] South West Research Institute. NASGRO reference manual version 8.1; 2016.
[58] McClung RC, Sehitoglu H. Characterization of fatigue crack growth in intermediate and large scale yielding. J Eng Mater Technol 1991;113(1):15–22.
[59] O'Connor S, Nowell D, Dragnevski K. Measurement of fatigue crack deformation on the macro- and micro-scale: Uniform and non-uniform loading. Int J Fatigue 2016;89:66–76.
[60] Pataky GJ, Sehitoglu H, Maier HJ. High temperature fatigue crack growth of haynes 230. Mater Charact 2013;75:69–78.
[61] Carroll J, Efstathiou C, Lambros J, Sehitoglu H, Hauber B, Spottswood S, et al. Investigation of fatigue crack closure using multiscale image correlation experiments. Eng Fract Mech 2009;76(15):2384–98.
[62] Rabbolini S, Beretta S, Foletti S, Rusconi L. Crack-closure measurements in low-cycle fatigue with digital image correlation. Mater Perform Characterizat 2016;5(3):232–48.
[63] Hos Y, Freire JL, Vormwald M. Measurements of strain fields around crack tips under proportional and non-proportional mixed-mode fatigue loading. Int J Fatigue 2016(89):87–98.
[64] Pommier S, Bompard P. Bauschinger effect of alloys and plasticity-induced crack closure: a finite element analysis. Fatigue Fract Eng Mater Struct 2000;23(2):129–40.
[65] Miller K. The short crack problem. Fatigue Fract Eng Mater Struct 1982;5(3):223–32.
[66] Dowling NE. Crack growth during low-cycle fatigue of smooth axial specimens. Astm Stp 1977;637:97–121. https://doi.org/10.1520/STP27990S.
[67] Rabbolini S, Beretta S, Foletti S, Riva A. Short crack propagation in LCF regime at room and high temperature in Q & T rotor steels. Int J Fatigue 2015;75:10–8. https://doi.org/10.1016/j.ijfatigue.2015.01.009.
[68] Forman RG, Shivakumar V. Growth behavior of surface cracks in the circumferential plane of solid and hollow cylinders. Fract mech seventeenth vol. West Conshohocken, PA: ASTM International; 1986. p. 59–74.
[69] Murakami Y, Endo M. Effect of hardness and crack geometries on ΔK, h of small cracks emanating from small defects. In: Miller K, Rios EDL, editors. The behaviour of short fatigue cracks. Mechanical Engineering Publications; 1986. p. 275–93.
[70] Zerbst U, Vormwald M, Pippan R, Gänser H-P, Sarrazin-Baudoux C, Madia M. About the fatigue crack propagation threshold of metals as a design criterion–a review. Eng Fract Mech 2016;153:190–243.
[71] Le VD, Pessard E, Morel F, Edy F. Influence of porosity on the fatigue behaviour of additively fabricated TA6V alloys. In: MATEC Web Conf, vol. 165; 2018. pp. 1–9. https://doi.org/10.1051/matecconf/201816502008.
[72] Zhu SP, Foletti S, Beretta S. Probabilistic framework for multiaxial LCF assessment under material variability. Int J Fatigue 2017;103:371–85. https://doi.org/10.1016/j.ijfatigue.2017.06.019.
[73] Romano S, Miccoli S, Beretta S. FE-based probabilistic analysis for fatigue assessment of AM parts. In: 1st ECCOMAS thematic conference on simulation for additive manufacturing, Munich; 2017.